An Ultraviolet–Optical Color–Metallicity Relation for Red Clump Stars Using *GALEX* and *Gaia*

Steven Mohammed[1], David Schiminovich[1], Keith Hawkins[2], Benjamin Johnson[3], Dun Wang[4], and David W. Hogg[4]

[1] Department of Astronomy, Columbia University, New York, NY 10027, USA; smohammed@astro.columbia.edu
[2] Department of Astronomy, The University of Texas at Austin, 2515 Speedway Stop C1400, Austin, TX 78712, USA
[3] Harvard-Smithsonian Center for Astrophysics, Cambridge, MA 02138, USA
[4] Center for Cosmology and Particle Physics, Department of Physics, New York University, New York, NY 10003, USA

Abstract

Although core helium-burning red clump (RC) stars are faint at ultraviolet wavelengths, their ultraviolet (UV)–optical color is a unique and accessible probe of their physical properties. Using data from the *Galaxy Evolution Explorer* All Sky Imaging Survey, *Gaia* Data Release 2, and the Sloan Digital Sky Survey Apache Point Observatory Galactic Evolution Experiment (APOGEE) DR14 survey, we find that spectroscopic metallicity is strongly correlated with the location of an RC star in the UV–optical color–magnitude diagram. The RC has a wide spread in $(NUV-G)_0$ color of over 4 mag compared to a 0.7 mag range in $(G_{BP}-G_{RP})_0$. We propose a photometric, dust-corrected, UV–optical $(NUV-G)_0$ color–metallicity [Fe/H] relation using a sample of 5,175 RC stars from APOGEE. We show that this relation has a scatter of 0.16 dex and is easier to obtain for large, wide-field samples than for spectroscopic metallicities. Importantly, the effect may be comparable to the spread in RC color attributed to extinction in other studies.

Key words: catalogs – Galaxy: general – stars: evolution – ultraviolet: stars

Supporting material: machine-readable table

1. Introduction

The Milky Way is host to a variety of stars spanning the entire stellar lifetime range. Average stars like our Sun eventually become red giants, some of which populate a prominent feature in color–magnitude diagrams (CMDs) called the red clump (RC), which consists of low-mass, metal-rich stars in the core helium-burning stage of stellar evolution. A sizable fraction of Solar neighborhood giants observed with *Hipparcos* are RC candidates (60%; Girardi 2016). Metallicities for these stars are readily available from surveys such as the Apache Point Observatory Galactic Evolution Experiment (APOGEE). The metallicity of RC stars can be used to understand the star formation history and ages of stars in the Milky Way and to inform stellar evolutionary models of RC, red giant, and horizontal branch stars (Girardi 2016). Populations of red giant stars that are at different distances will populate different regions of [α/Fe] versus [Fe/H] space and will even show some bimodality between high- and low-[α/Fe] stars in regions above the disk (Hayden et al. 2015).

Color is a proxy for the effective temperature. T_{eff} and the luminosity of an RC star remain relatively constant throughout most of its life. T_{eff} is dependent on the initial mass of the RC star (Girardi 2016, see their Figure 1(a)) and will also depend on the metallicity. For an RC star of a given stellar mass, the luminosity varies with the metallicity. Stars with a higher luminosity will have a lower metallicity and vice versa (Girardi 2016).

Several attempts to relate photometric measurements to metallicities have been made. Ruiz-Dern et al. (2018) use photometry from *Gaia* DR1, *Hipparcos*, Tycho 2, Two Micron All-Sky Survey (2MASS0), the American Association of Variable Star Objects (AAVSO) Photometric All-Sky Survey (APASS), DR9, and the *Wide-field Infrared Survey Explorer* and metallicities from various sources to calibrate a dereddened Hertzsprung–Russell (HR) diagram. Ivezić et al. (2008) attempted to create a metallicity map of the Milky Way using only Sloan Digital Sky Survey (SDSS) photometry that have similar metallicity errors to those measured from SDSS spectra. Cole et al. (2000) used Strömgren vby photometry to obtain a color–metallicity relation for red giants in the Large Magellanic Cloud and found that it is comparable with their spectroscopic results but is also practically useful for quickly obtaining metallicities for many objects.

With the release of *Gaia* DR2 (Gaia Collaboration et al. 2018a), the Milky Way can now be probed to greater depths than ever before. The *Gaia* DR2 release presents parallax measurements for over 1 billion stars, which provide crucial distance information and *G*-band measurements to allow for construction of the CMD of the Milky Way field population. We combine near-ultraviolet (NUV)-band data from the *Galaxy Evolution Explorer* (*GALEX*) All Sky Imaging Survey (GAIS; Martin et al. 2005) with *Gaia* and a catalog of RC stars from APOGEE DR14 (Ting et al. 2018). RC stars are very faint in NUV and should separate clearly from the main sequence. As RC stars have not been extensively probed in the UV, this study has the potential to strengthen our understanding of the relation between UV–optical colors and the physical properties of stars in this core helium-burning stage. In this paper, we focus on an $(NUV-G)_0$ color–metallicity relation and show how it compares to a similar color–metallicity relation derived using optical colors. Finally, we also discuss how this relation compares to predictions from stellar evolutionary model tracks, using the Modules for Experiments in Stellar Astrophysics (MESA) Isochrones and Stellar Tracks (MIST) code (Paxton et al. 2011, 2013, 2015; Choi et al. 2016; Dotter 2016).

2. Observations

2.1. Red Clump Data

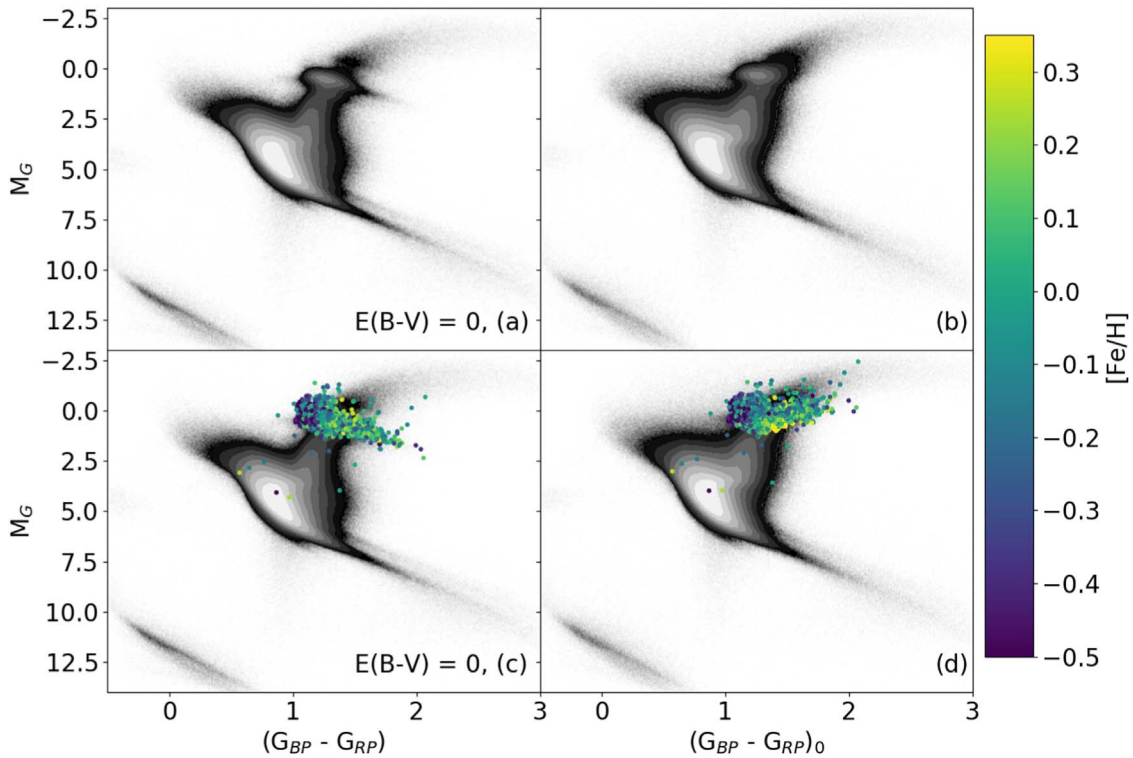We build a sample of 5,175 RC stars from Ting et al. (2018), which is constructed using data from the APOGEE

Figure 1. M_G vs. (NUV–G)$_0$ distribution for the full parallax-selected (<3.5 kpc) GAIS–*Gaia* catalog (top panels) with matches with RC stars shown (bottom panels). The left panels show the CMD without a Galactic extinction correction, and the right panels apply a correction as described in the text. The main locus at the center of each panel shows the main sequence. The RC stars are overlaid and colored by [Fe/H]. There is a clear trend of metallicity with NUV–G color in both cases. [Fe/H] from APOGEE DR14.

(Majewski et al. 2017) and Large Sky Area Multi-Object Fibre Spectroscopic Telescope (LAMOST, Xiang et al. 2017) surveys. Ting et al. (2018) built an RC sample of Milky Way stars from APOGEE DR14 data with ∼3% contamination from red giant stars. For our analysis, we only used the pristine RC sample obtained from APOGEE spectra. From its high signal-to-noise, near-infrared (1.51–1.70 μm) spectra, derived parameters, such as metallicities, $T_{\rm eff}$, and log g parameters, are available, as well as abundances for many elements. APOGEE elemental abundances are typically accurate to 0.2 dex over the metallicity range considered here (García Pérez et al. 2016).

2.2. GAIS and Gaia DR2

GAIS contains NUV data for millions of objects across the entire sky. Gaia DR2 provides *Gaia* G, G$_{BP}$, and G$_{RP}$ magnitudes and parallaxes that can be used to obtain distance information. The errors in G, $G_{\rm BP}$, and $G_{\rm RP}$ are of the order of millimagnitudes. We apply a small error-dependent correction to the *Gaia* parallaxes (Lutz & Kelker 1973; Oudmaijer et al. 1998). We then invert the parallax to get a distance. To cross-match these data, we use the astropy (Astropy Collaboration et al. 2013) function *search around sky* with a search radius of 3 arcseconds. In total, we utilize coverage in *GALEX* NUV, *Gaia* G, G$_{\rm BP}$, G$_{\rm RP}$, and the relevant APOGEE footprint.

Galactic extinction plays a much larger role for the NUV than the other bands (Cardelli et al. 1989) and will have a nontrivial effect on the location of objects in a CMD. To account for this reddening, we use the 3D dust map from Green et al. (2015), which gives E_{B-V} as a function of distance, in conjunction with *Gaia* parallax-derived distances to estimate the reddening in the line of sight of each object in this catalog. The NUV–G color is dust corrected (indicated by a "0" subscript) using these E_{B-V}

values, adopting $R_{\rm NUV}$ from Yuan et al. (2013) and R_G from Jordi et al. (2010), who obtain R_G values between 2.4 and 3.6. For our analysis, the extinction corrections for NUV and G are NUV$_0$ = NUV − E_{B-V} × 7.24 and G_0 = G − E_{B-V} × 2.85. We are restricted to the sky coverage of the Green et al. (2015) map and remove any objects in the GAIS–*Gaia* catalog that do not overlap with the map.

For the final catalog, we make several additional cuts to the data. The final catalog contains objects that have detections in NUV, G, $G_{\rm BP}$, and $G_{\rm RP}$; [Fe/H] and $T_{\rm eff}$ measurements; parallax errors less than 10%, *visibility_periods_used* > 8; and distances less than 3500 pc. Additionally, we use the *RC_Pristine* classification from Ting et al. (2018). We do not require the APOGEE flags to be set to 0 for these objects (65 in total); however, the removal of these objects does not impact our results. Our final catalog of GAIS and *Gaia* objects contains 10,357,542 objects. We cross-match this catalog with the RC catalog and obtain 5,175 matches.

GAIS–*Gaia* does not appear to be limited to only very blue objects despite the expectation that *GALEX* would not observe many red stars. There is a large population at the expected position of the RC in the CMD. There are about 91% of objects in the main catalog along the main sequence versus 4% of objects in the RC.

3. Results

Figures 1 and 2 show UV–optical and optical CMD histograms for the GAIS–*Gaia* catalog, using both uncorrected and Galactic extinction-corrected magnitudes. The general shape of the UV–optical CMD is very similar to that of the optical: a large main sequence with the red giant branch and RC prominently displayed. The main sequence stretches from
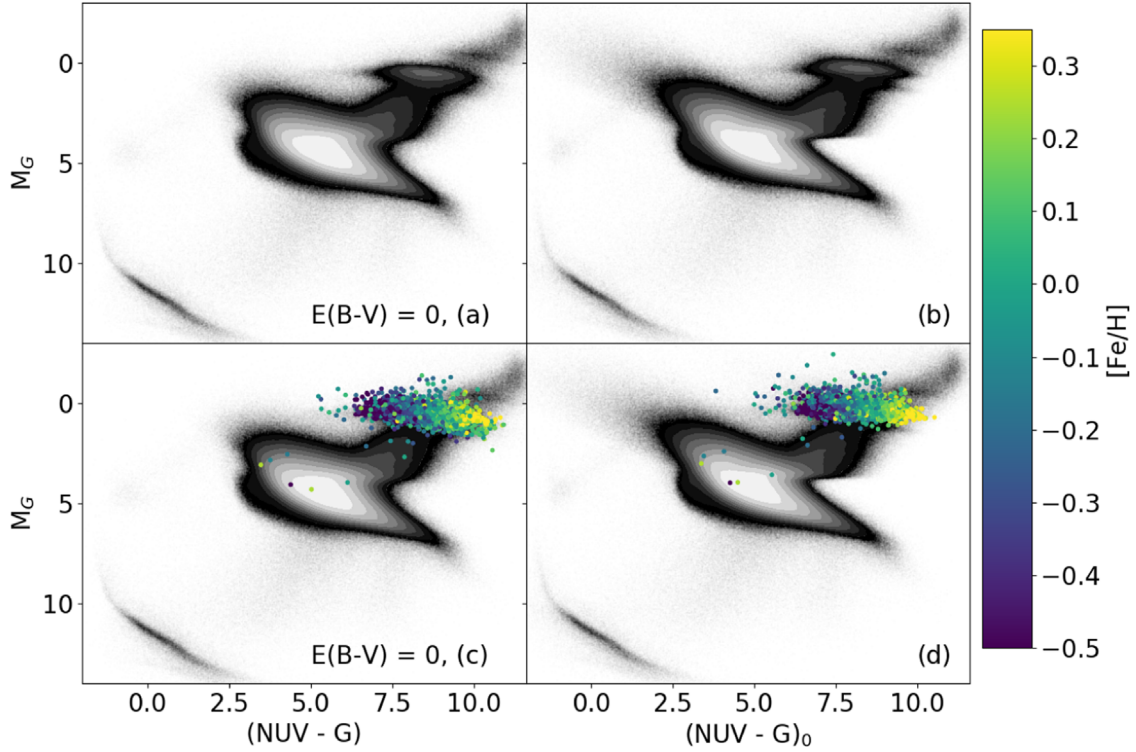
Figure 2. M_G vs. G_{BP}–G_{RP} distribution for the full GAIS–*Gaia* catalog (top panels) that matches with RC stars shown (bottom panels). The left panels show the CMD without a Galactic extinction correction, and the right panels applies a correction as described in the text.

Table 1
Values for the 5,175 Objects in This Sample

R.A. (°)	Decl. (°)	NUV (mag)	$(NUV–G)_0$ (mag)	G_{BP} (mag)	$(G_{BP}–G_{RP})_0$ (mag)	$E(B–V)$ (mag)	DM (mag)	[Fe/H]	T_{eff} (K)	$[\alpha/Fe]$
0.1300	15.2717	18.11 ± 0.03	7.46 ± 0.03	11.17 ± 0.00	1.16 ± 0.00	0.04	10.41	-0.41 ± 0.01	4931.00	0.10 ± 0.02
0.2081	16.3654	19.40 ± 0.07	8.82 ± 0.07	11.18 ± 0.00	1.31 ± 0.00	0.04	10.13	0.06 ± 0.01	4699.00	0.01 ± 0.01
0.3194	15.3927	19.49 ± 0.06	9.78 ± 0.06	10.36 ± 0.00	1.39 ± 0.00	0.04	9.10	0.34 ± 0.01	4553.00	0.02 ± 0.01
0.4016	0.2359	18.97 ± 0.04	8.80 ± 0.04	10.74 ± 0.00	1.26 ± 0.00	0.02	9.61	0.04 ± 0.01	4723.00	-0.01 ± -0.42
0.5204	15.0377	19.08 ± 0.05	7.55 ± 0.05	12.04 ± 0.00	1.17 ± 0.00	0.05	11.27	-0.36 ± 0.01	4915.00	0.13 ± 0.02
0.6003	16.4273	17.30 ± 0.02	7.94 ± 0.02	9.90 ± 0.00	1.20 ± 0.00	0.03	9.03	-0.24 ± 0.01	4826.00	0.03 ± 0.02
0.6012	16.9140	19.10 ± 0.06	8.48 ± 0.06	11.18 ± 0.00	1.24 ± 0.00	0.03	10.17	-0.01 ± 0.01	4782.00	0.03 ± 0.06
0.6975	17.1347	17.58 ± 0.03	8.38 ± 0.03	9.77 ± 0.00	1.24 ± 0.00	0.03	9.25	-0.23 ± 0.01	4734.00	0.02 ± 0.01
0.9191	16.9788	18.68 ± 0.05	8.95 ± 0.05	10.37 ± 0.00	1.37 ± 0.00	0.03	9.18	0.17 ± 0.01	4548.00	0.05 ± 0.04
0.9634	75.8578	19.44 ± 0.34	8.37 ± 0.34	11.79 ± 0.00	1.53 ± 0.00	0.30	10.67	0.15 ± 0.01	4929.00	-0.01 ± -0.01

Note. (1) *Gaia* R.A., (2) *Gaia* decl., (3) *GALEX* NUV, (4) dust-corrected NUV–G, (5) Gaia G_{BP}, (6) dust-corrected G_{BP}–G_{RP}, (7) $E(B–V)$ from Green et al. (2015), (8) distance modulus, (9) stellar metallicity, (10) effective temperature from APOGEE $\pm$ 91.47 K for all values, and (11) alpha abundance. Table 1 is published in its entirety in the machine-readable format. A portion is shown here for guidance regarding its form and content.

(This table is available in its entirety in machine-readable form.)

$(NUV–G)_0 = 8$ and $M_G = 6$ to $(NUV–G)_0 = 2.5$ and $M_G = 1$ and is where the bulk of the survey matches appear. The secondary locus around $(NUV–G)_0 = 8$ and $M_G = 0$ (Hawkins et al. 2017) is populated by red giants, notably RC stars. The spread of the entire RC in $(NUV–G)_0$ is unlike that seen in $(G_{BP}–G_{RP})_0$, spreading over 4 mag compared to a spread of 0.7 mag in $(G_{BP}–G_{RP})_0$, as shown in Figure 2. The spread could be due to the age, metallicity, and extinction of the RC stars. As discussed further below, our optical CMD is similar to that of Gaia Collaboration et al. (2018b), which shows the appearance of an RC for low extinction sources ($E(B–V) < 0.015$) in DR2.

We show a portion of our catalog-matched RC sample in Table 1. In Figures 1 and 2, we overplot this sample in the bottom panels. The RC stars show a clear NUV–optical color-dependent trend with [Fe/H] (higher [Fe/H] at redder $(NUV–G)_0$ and vice versa, shown in Figure 1). This spread is unique to $(NUV–G)_0$ color, especially when the dust correction is applied. In Figure 3, we show the distributions for the RC stars of the Galactic longitude, distance, NUV magnitude, and $E(B–V)$. The $E(B–V)$ for most of this sample is less than 0.1, suggesting relatively small extinction corrections. Most of the RC sample is between $18 < NUV < 20$. The GAIS survey limit is 21 (5σ), indicating that this sample is reasonably complete out to our distance limit.

Using the derived parameters from APOGEE, in Figure 4 we show that the RC UV–optical color also correlates with the effective temperature. The trend for $(G_{BP}–G_{RP})_0$ is much weaker
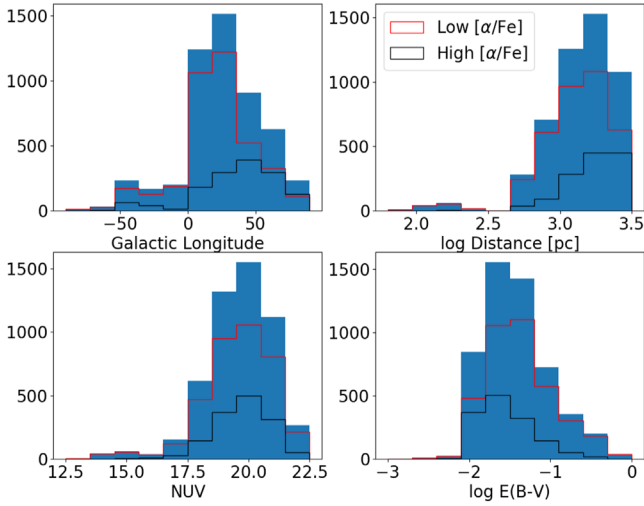
Figure 3. Various statistics for our GAIS–*Gaia* RC sample. The sample is mostly restricted to the upper Galactic plane and at distances greater than 500 pc. We also overplot the low- and high-[α/Fe] populations discussed further below.
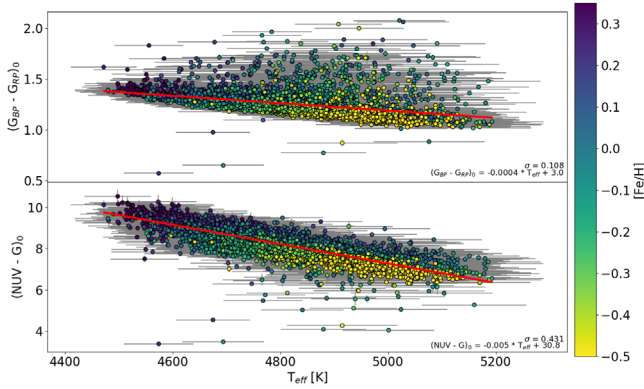

Figure 4. $T_{\rm eff}$ from APOGEE vs. extinction-corrected $(G_{\rm BP}-G_{\rm RP})_0$ and $(NUV-G)_0$ colored by [Fe/H] for our RC sample. $(G_{\rm BP}-G_{\rm RP})_0$ shows significant scatter. $(NUV-G)_0$ is more tightly correlated with $T_{\rm eff}$, although we also identify a subpopulation of very blue outliers.

and more highly scattered. From a line fit, we measure $\sigma_{(BP-RP)_0} = 0.11$ and $\sigma_{(NUV-G)_0} = 0.43$. Compared to the slope of the RC in each color, the relative scatter is 3.3 times smaller in $(NUV-G)_0$ than in $(G_{\rm BP}-G_{\rm RP})_0$. If we simply look at the coefficient of determination, $r^2_{(BP-RP)_0} = 0.15$ while $r^2_{(NUV-G)_0} = 0.66$.

4. Discussion

4.1. Spectroscopic Catalog-matched Sample

In this section, we define a UV–optical color–metallicity relation. First we separate our RC sample into two subsamples of low- and high-[α/Fe] stars. Figure 5 shows [α/Fe] versus [Fe/H] and distinguishes between low- and high-[α/Fe] stars using a simple cut in [α/Fe] and [Fe/H] (Nidever et al. 2014; Hawkins et al. 2015; Li et al. 2018). This cut is qualitative and is only used to distinguish the two loci of points. The equation used to find the high-[α/Fe] stars is

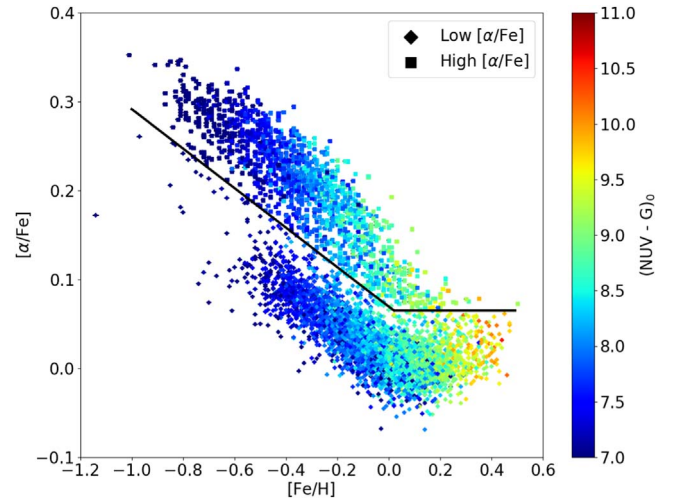$$[\alpha/{\rm Fe}] > \begin{cases} -0.22 \times [Fe/H] + 0.069 & \text{if } [{\rm Fe/H}] < 0.02 \\ 0.065 & \text{if } [{\rm Fe/H}] > 0.02 \end{cases}. \quad (1)$$

Figure 5. [α/Fe] vs. [Fe/H] colored by the dust-corrected $(NUV-G)_0$ (described in Figure 1). Hawkins et al. (2015) discuss a cartoon depiction of this trend separating the lower branch (low-[α/Fe] stars) from the upper branch (high-[α/Fe] stars). The lines drawn here are just a qualitative cut based on the emergence of two different populations combined with work from Hawkins et al. (2015).

The high-[α/Fe] stars overall have a much higher [α/Fe], especially at lower [Fe/H]. The [α/Fe]–Fe/H relation is a unique way to separate different Galactic components to understand the star formation history of different parts of the Milky Way. The low-[α/Fe] stars are thought to be considerably younger than the high-[α/Fe] stars because of the smaller amount of α elements (O, Mg, Si, Ca, and Ti) for a given [Fe/H]. We see the same separation as in Nidever et al. (2014) between the low and high α sequence around [Fe/H] = 0.2.

The majority of high-[α/Fe] stars are bluer than the low-[α/Fe] subsample. Alternatively, at a given $(NUV-G)_0$, the high-[α/Fe] stars have a lower [Fe/H] than their low-[α/Fe] counterparts. While none of the low-[α/Fe] stars are metal-poor enough to be considered halo stars (typically with metallicities of [Fe/H] < −0.5), they are not significantly different from the entire sample in other quantities except [α/Fe]. The trends for the two different populations presented in Figure 5 suggest different color–metallicity relations between them.

In Figure 6, we show a clear trend between the $(NUV-G)_0$ color and metallicity for the full sample that spans a wider range of colors than in optical wavelengths, as shown in Figure 1. This relation becomes much tighter when an extinction correction is added. We also separate the two low- and high-[α/Fe] populations in the middle and bottom panels, respectively. We obtain the following relationship for the full extinction-corrected sample:

$$[{\rm Fe/H}] = 0.256\,(NUV - G)_0 - 2.204. \quad (2)$$

The standard deviation from the linear fit is $\sigma_{\rm [Fe/H]} \sim 0.16$ dex. Equation (1) provides a new means to determine metallicity from photometry with a precision similar to low-resolution spectroscopy (e.g., SDSS Sloan Extension for Galactic Understanding and Exploration (SEGUE); Lee et al. 2011, where they measure [Fe/H] to a precision of 0.23 dex) but at a much cheaper cost and can be obtained for many more stars. The standard deviations of the fits to the low- and high-[α/Fe] subsamples are 0.146 and 0.12, respectively. If we fit $T_{\rm eff}$ to model [Fe/H] instead of $(NUV-G)_0$, we get standard deviations for the full, low-, and high-[α/Fe] samples of 0.192, 0.154, and 0.111, with the first two being larger than their $(NUV-G)_0$ fit counterparts
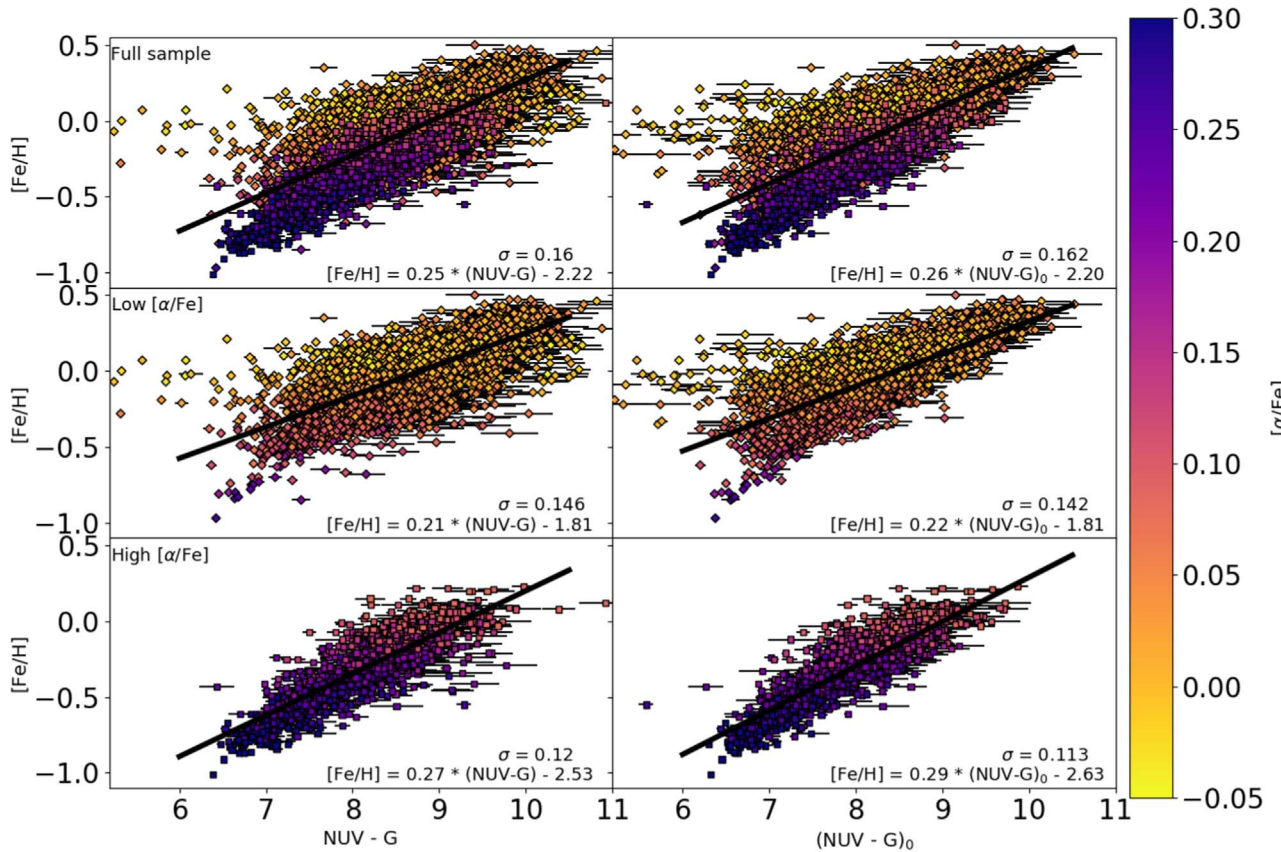
Figure 6. [Fe/H] vs. (NUV–G)$_0$ colored by [α/Fe] without (left) and with (right) a Galactic extinction correction. We find several outliers at (NUV–G)$_0$ < 6. One suggestion is that these objects are binaries but that is uncertain. What we do know is that these objects populate a region in the CMD space that is outside of the typical RC population seen in Figure 1. The middle panels show low-[α/Fe] stars, and the bottom panels show high-[α/Fe] stars. Each fit is done only on the data in that panel. We include all six fits in their corresponding panels. The (NUV–G)$_0$ spread over 4 mag is much greater than in optical colors. The color–metallicity relation has a weak dependence on [α/Fe]. The trend tightens when corrected for Galactic extinction.

and the high-[α/Fe] standard deviation being roughly the same. The coefficient of determination of all three are 0.58, 0.56, and 0.74, respectively.

The two different low- and high-[α/Fe] populations from Figure 5 appear to have different color–metallicity relations. High-[α/Fe] stars have much less scatter from the relation than low-[α/Fe] stars, and the slope is higher in the high-[α/Fe] color–metallicity relation. At the very metal-poor end ([Fe/H] < −0.6), RC stars appear to be a part of the galaxy's thick disk (Brook et al. 2012; Hawkins et al. 2015), and as can been seen from Figure 5, they are bluer objects in general. The low-[α/Fe] population also shows objects that are bluer than expected, including several outliers that are bluer than (NUV–G)$_0$ < 6, some of which could be binaries. We will leave a more detailed discussion of these outliers to future papers. Even with the presence of outliers, the overall relation is still about as precise as spectroscopy. If we apply the same analysis to just the Bovy et al. (2014) sample (which the Ting et al. 2018 sample does contain), then we get a standard deviation of $\sigma = 0.12$. This is better than the full sample but uses only 208 objects to fit versus our full sample. The scatter in the relation and overall shape of Δ[Fe/H] is still very similar to that of the full sample.

4.2. Photometrically Selected Sample

To demonstrate the effectiveness of this color–metallicity relation, we select a subset of photometrically defined RC stars from the CMD in Figure 1. We define our RC box as bound at

6 > (NUV–G)$_0$ > 10.5 and 0.9 > M_G > −0.1. This region contains many possible RC candidates from which one can also derive asteroseismic parameters with minimal contamination from red giant branch stars using the methods in Hawkins et al. (2018). The main source of the bias comes from uncertainties in NUV, which would restrict the range of objects detectable by *GALEX*. If we assume the contamination in our new CMD cut sample is greater and only use this color cut to define our RC stars, we can see how well this choice of box limits performs. We apply ASPCAPFLAG = 0 and log g < 3 to our catalog and get a subsample of 4,656 RC stars, or 90%.

We apply the same cuts as described in Section 2.2 to a matched catalog between GAIS, *Gaia* DR2, and APOGEE DR14 and replot the [Fe/H] - (NUV–G)$_0$ relation with these data in Figure 7. The overall trend between UV–optical color and metallicity closely matches that of the spectroscopically obtained RC sample. The scatter in the relation is larger, but this is likely due to contamination from other giant stars. There is an offset at (NUV–G)$_0$ < 8 for the highest-[α/Fe] stars, which likely is due to the steeper relation for the high-[α/Fe] stars in this sample. If we fit this test sample but separate them by their low- and high-[α/Fe] components, we get standard deviations of 0.21, 0.21, and 0.16 for the whole, low-, and high-[α/Fe] samples, respectively. As seen in Figure 6, the high-[α/Fe] subsample tends to model the data better.

Photometric–metallicity relations have been calculated or observed in the past. For example, Ivezić et al. (2008) used F
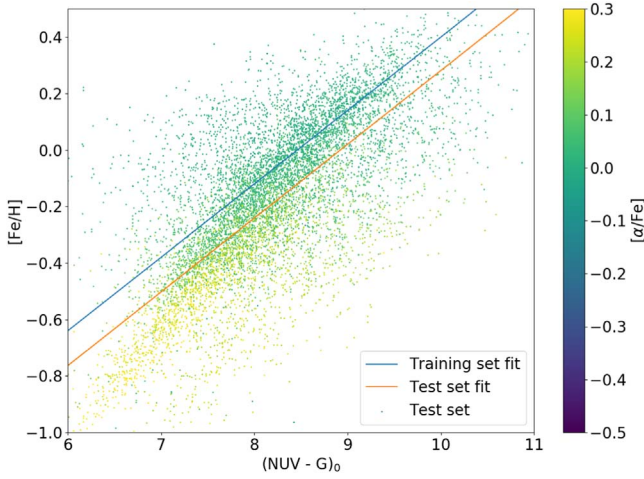
Figure 7. [Fe/H] vs. (NUV–G)$_0$ for stars within the RC box described in the text. The blue line is the dust-corrected fit for the entire sample from Figure 6 top right panel, while the orange line is the fit to the test set. The data match the trend we see at (NUV–G)$_0 > 7.5$. The slopes of the fits are the same with an offset in the y-intercept.
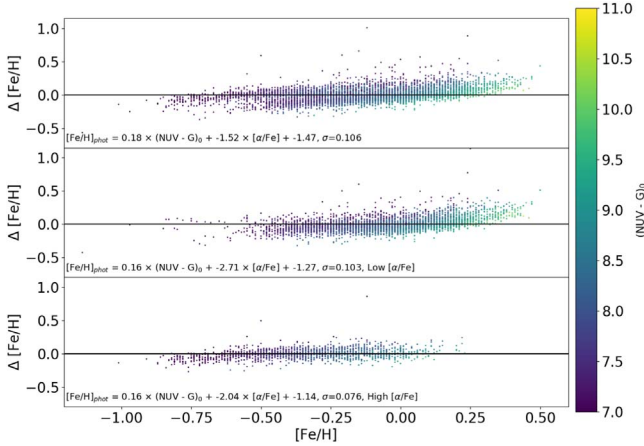

Figure 8. [Fe/H] vs. (NUV–G)$_0$ using a fit that includes a linear [α/Fe] term.

Figure 9. (a) log g histogram of our catalog showing a peak around 2.4. (b) log g vs. log($T_{\rm eff}$). We see a clear trend relating log g, $T_{\rm eff}$ with [Fe/H].

and G main-sequence stars to derive a relation between [Fe/H], u–g, and g–r. The u–g color, or the UV excess, depends on the metallicity because of the high absorption of metals at bluer colors, affecting the star's flux. This UV excess depends on the g–r color, which is related to the star's effective temperature. RC stars are known to have a flux–temperature relation that varies greatly depending on the metallicity. Metal line blanketing may also play a role due to the high-[Fe/H] values in this sample (Choi et al. 2016; Girardi 2016). Metals in stellar atmospheres absorb blue light due to metal line blanketing and should show significant absorption in bluer wavelengths like NUV. In our sample, these metal-rich stars are the reddest, with (NUV–G)$_0$ values reaching up to 10 mag versus the blue end at (NUV–G)$_0 = 6$, which contains the most metal-poor stars (Figure 6). Due to their similarity, these trends may also hold for stars along the giant branch, albeit with an increased scatter within our empirical data due to the different physical properties between the whole range of giant branch stars versus the narrow RC. We attempted to model this photometric–metallicity relation using [α/Fe] terms in a variety of ways (similar to the method in Ivezić et al. 2008), one of which i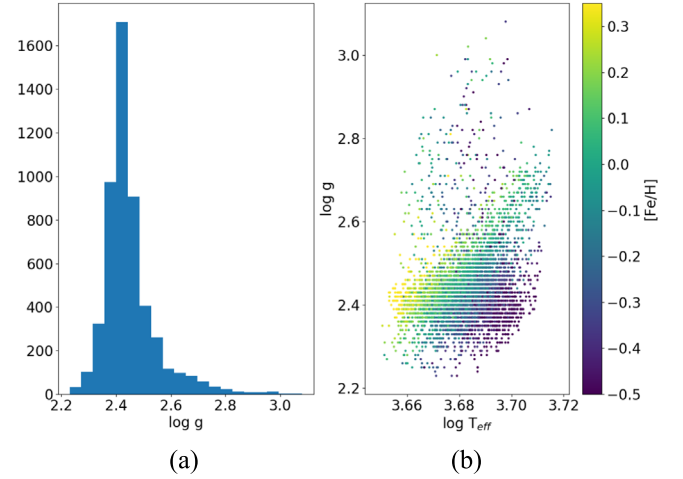s shown in Figure 8. The fits that use [α/Fe] are not significantly better than our relation that uses only a linear (NUV–G)$_0$ term.

4.3. Comparison to Models

Finally we explore how our relation compares to predictions from a recently developed stellar evolutionary code. The MIST model provides tracks and photometric outputs for a full range of stellar masses and metallicities with sufficient resolution to follow short-lived evolutionary stages (Choi et al. 2016). We used evolutionary tracks for the range of masses (1 to 2.5 M$_\odot$) and metallicities ($-1.0 <$ [Fe/H] < 0.4; 0.25 dex steps) likely to appear in the Milky Way field RC population. Our models assume Solar abundances, and therefore, do not include a range of alpha enhancement. Luminosities were calculated in G, $G_{\rm BP}$, $G_{\rm RP}$, and NUV bands, using the most up to date *Gaia* bandpasses. We applied a photometric selection to the final outputs, selecting stars in a similar region for the RC in the CMD, as described above, while also restricting the model to the core helium-burning phase (MESA EEP 631–707). These cuts allow for a wide range of stellar masses, but we find that the metallicity versus NUV–G color relation in the models is only weakly dependent on the initial mass and age during this stage. Our selection cuts also include at least part of the region of the CMD known as the "secondary RC" though we leave discussion of the distinct RC to future work. In Figures 10 and 11, we plot NUV versus [Fe/H] colored by $T_{\rm eff}$ and log g, respectively. The extinction-corrected fits for the full sample and the high-[α/Fe]-only subsample are shown on both plots.

The linear fits in Figure 10 provide a good match to the models over most of the metallicity range of our RC sample. Bluer stars tend to be hotter and have a lower metallicity and vice versa. The fit lines overlap models with the $T_{\rm eff}$ range in Figure 4. Figure 9 shows that our mean fits are consistent with models with log $g \sim 2.4$, with high-[α/Fe] stars that have a slightly lower log g (and $T_{\rm eff}$) at a fixed metallicity, though the difference in log g between the mean of the two populations is very small (about 0.05). The larger scatter with an increasing metallicity in the models is also seen in Figure 6, most notably in the low-[α/Fe] subsample. The scatter can be at least partially explained by the scatter seen in the stellar evolution models for a range of stellar masses and ages. Other factors, such as errors in Galactic extinction, binarity, and a range of
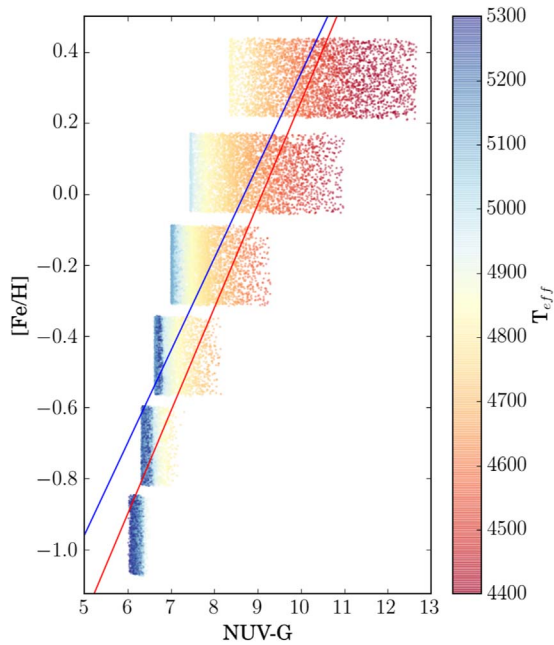
Figure 10. Figure 6 plotted with MIST stellar evolution models colored by T_{eff}. The blue line is the fit of the entire sample, and the red line is the fit of only the high-[α/Fe] stars. Models are calculated using cuts described in the text at discrete initial metallicities, spaced by 0.25 dex, though the bands in the plots are dithered for clarity. These plots are purely illustrative of the spread of the color vs. metallicity vs. mass, etc. They do not correct or cut based on the lifetime of the star in each evolutionary phase, and therefore, overrepresent some parts of the population.
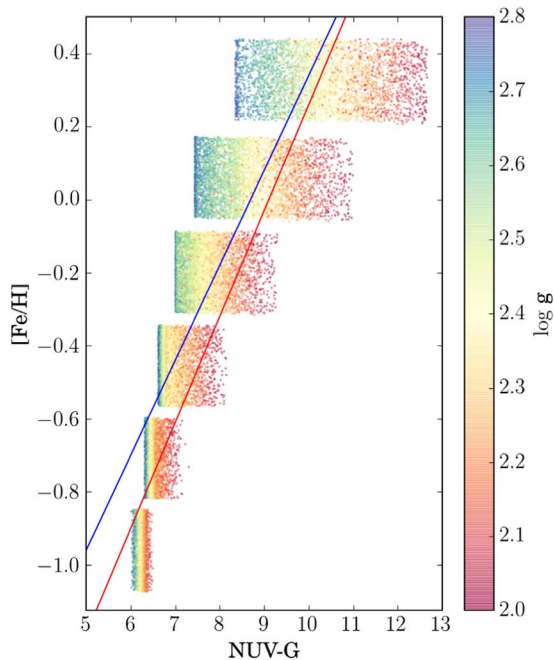

Figure 11. Figure 6 plotted with MIST stellar evolution models colored by log g. The blue and red lines and dithering of points for clarity are the same as in Figure 10.

alpha enhancements may also contribute to the scatter. This topic will be studied in future papers.

RC stars are used as standard candles in infrared due to their constant absolute magnitude and color. The metallicity, mass, age, and extinction make their use as standard candles difficult in bluer

wavelengths. Using the color–metallicity relation, we can create a metallicity map of the Galaxy (e.g., Önal Taş et al. 2016) and increase the accuracy of RC stars as standard candles. These results also have implications on the use of RC stars as extinction probes. Yanchulova Merica-Jones et al. (2017) use *Hubble Space Telescope* observations that extend to the NUV and explain the spread in color as due to extinction. They conclude the RC is confined to a small region in the CMD with similar metallicities. Instead, we see a large spread in $(\mathrm{NUV}–G)_0$ with a range of metallicities, indicating that the metallicity may play a nontrivial role in understanding the RC in the CMD space. Their use as extinction probes and in extinction mapping (seen in Girardi 2016 in areas such as the Large Magellanic Cloud and the Milky Way bulge) will vary depending on the star's metallicity and age, affecting the assumption that there is no systematic variation in intrinsic RC properties.

5. Conclusion

Using a sample of 5,175 RC stars from APOGEE with data from *GALEX* and *Gaia*, we identify the RC in the UV–optical CMD space, as well as the existence of a color–metallicity relation that is tighter in $(\mathrm{NUV}–G)_0$ than $(G_{\mathrm{BP}}–G_{\mathrm{RP}})_0$. We see a strong dependence of color on T_{eff} and the metallicity. As part of this analysis, we apply a Galactic extinction correction using a 3D dust map from Green et al. (2015) and *Gaia* distances, which further tightens the relation. If we separate the sample into low- and high-[α/Fe] stars, high-[α/Fe] stars appear bluer than their low-[α/Fe] counterparts for a given temperature and redder at a fixed metallicity. Finally, we find a tight relation between $(\mathrm{NUV}–G)_0$ and [Fe/H] with a standard deviation of about $\sigma = 0.16$ that can be used to estimate stellar metallicities of RC stars when a spectroscopic metallicity measurement is missing. This relation will be used to obtain photometric metallicities from other stars in the same CMD space as RC candidates using only their UV–optical color. An NUV *GALEX* Plane Survey (S. Mohammed et al. 2018, in preparation) will provide NUV measurements for the Galactic Plane for the first time using *GALEX*. This survey will provide millions of new objects brighter than NUV = 20 mag that will aid in RC investigations, as well as many other fields in Galactic astronomy. A spectroscopic follow-up of these candidates could confirm their RC status using the method of Hawkins et al. (2018) and Ting et al. (2018) and allow us to further understand the UV–optical color–metallicity–age relation. RC stars are excellent extinction probes, and if their metallicity is known, it is enough to use a CMD to fit for its extinction values. Using our color–metallicity relation in conjunction with extinction measurements from Green et al. (2015), we can narrow the variables to the mass and age.

ORCID iDs

David W. Hogg ⓘ https://orcid.org/0000-0003-2866-9403

References

Astropy Collaboration, Robitaille, T. P., Tollerud, E. J., et al. 2013, A&A, 558, A33
Bovy, J., Nidever, D. L., Rix, H.-W., et al. 2014, ApJ, 790, 127
Brook, C. B., Stinson, G. S., Gibson, B. K., et al. 2012, MNRAS, 426, 690
Cardelli, J. A., Clayton, G. C., & Mathis, J. S. 1989, ApJ, 345, 245
Choi, J., Dotter, A., Conroy, C., et al. 2016, ApJ, 823, 102
Cole, A. A., Smecker-Hane, T. A., & Gallagher, J. S., III 2000, AJ, 120, 1808
Dotter, A. 2016, ApJS, 222, 8
Gaia Collaboration, Babusiaux, C., van Leeuwen, F., et al. 2018b, A&A, 616, A10
Gaia Collaboration, Brown, A. G. A., Vallenari, A., et al. 2018a, A&A, 616, A1
García Pérez, A. E., Allende Prieto, C., Holtzman, J. A., et al. 2016, AJ, 151, 144
Girardi, L. 2016, ARA&A, 54, 95
Green, G. M., Schlafly, E. F., Finkbeiner, D. P., et al. 2015, ApJ, 810, 25
Hawkins, K., Jofré, P., Masseron, T., & Gilmore, G. 2015, MNRAS, 453, 758
Hawkins, K., Leistedt, B., Bovy, J., & Hogg, D. W. 2017, MNRAS, 471, 722
Hawkins, K., Ting, Y.-S., & Walter-Rix, H. 2018, ApJ, 853, 20
Hayden, M. R., Bovy, J., Holtzman, J. A., et al. 2015, ApJ, 808, 132
Ivezić, Ž, Sesar, B., Jurić, M., et al. 2008, ApJ, 684, 287
Jordi, C., Gebran, M., Carrasco, J. M., et al. 2010, A&A, 523, A48
Lee, Y. S., Beers, T. C., Allende Prieto, C., et al. 2011, AJ, 141, 90
Li, C., Zhao, G., Zhai, M., & Jia, Y. 2018, ApJ, 860, 53
Lutz, T. E., & Kelker, D. H. 1973, PASP, 85, 573
Majewski, S. R., Schiavon, R. P., Frinchaboy, P. M., et al. 2017, AJ, 154, 94
Martin, D. C., Fanson, J., Schiminovich, D., et al. 2005, ApJL, 619, L1
Nidever, D. L., Bovy, J., Bird, J. C., et al. 2014, ApJ, 796, 38
Önal Taş, Ö., Bilir, S., Seabroke, G. M., et al. 2016, PASA, 33, e044
Oudmaijer, R. D., Groenewegen, M. A. T., & Schrijver, H. 1998, MNRAS, 294, L41
Paxton, B., Bildsten, L., Dotter, A., et al. 2011, ApJS, 192, 3
Paxton, B., Cantiello, M., Arras, P., et al. 2013, ApJS, 208, 4
Paxton, B., Marchant, P., Schwab, J., et al. 2015, ApJS, 220, 15
Ruiz-Dern, L., Babusiaux, C., Arenou, F., Turon, C., & Lallement, R. 2018, A&A, 609, A116
Ting, Y.-S., Hawkins, K., & Rix, H.-W. 2018, ApJL, 858, L7
Xiang, M.-S., Liu, X.-W., Yuan, H.-B., et al. 2017, MNRAS, 467, 1890
Yanchulova Merica-Jones, P., Sandstrom, K. M., Johnson, L. C., et al. 2017, ApJ, 847, 102
Yuan, H. B., Liu, X. W., & Xiang, M. S. 2013, MNRAS, 430, 2188